Dalton Transactions

Accepted Manuscript

ROYAL SOCIETY OF CHEMISTRY

www.rsc.org/dalton

Highlights

- Cobalt orthosilicate (CSO) as active material for secondary lithium-ion batteries.
- A lithium storage mechanism in CSO is proposed based on *in situ* XRD combined with *ex situ* XPS and SEM studies
- Initially formed metallic cobalt enables the reversible formation of lithium silicate.
- CSO-based electrodes reveal a highly stable cycling behavior and a good high rate performance.

Cobalt Orthosilicate as New Electrode Material for Secondary Lithium-Ion Batteries

Franziska Mueller [1,2], Dominic Bresser [1,2,*], Nathalie Minderjahn [1], Julian Kalhoff [1], Sebastian Menne [1], Steffen Krueger [1], Martin Winter [1], Stefano Passerini [1,2,*]

[1] *Institute of Physical Chemistry & MEET Battery Research Centre, University of Muenster, Corrensstr. 28/30& 46, 48149 Muenster, Germany*

[2] *Helmholtz Institute Ulm, Karlsruher Institute of Technology, Albert-Einstein-Allee 11, 89081 Ulm, Germany*

Abstract

Herein, cobalt orthosilicate (Co_2SiO_4, CSO) is presented as a new electrode material for rechargeable lithium-ion batteries. Orthorhombic α-Co_2SiO_4 (space group: *Pbnm*) was synthesized by a conventional solid-state method and subsequently characterized using X-ray diffraction (XRD) and scanning electron microscopy (SEM). To study the reversible lithium uptake and release cyclic voltammetry (CV), *in situ* XRD, as well as *ex situ* X-ray photoelectron spectroscopy (XPS) and SEM analysis were performed. Based on these results a new reaction mechanism is proposed including the reversible formation of lithium silicate. In addition, the electrochemical performance of CSO-based electrodes was investigated by galvanostatic cycling, applying varying specific currents. Such electrodes revealed a good high rate capability and a highly reversible cycling behavior, providing a specific capacity exceeding 650 mAh g^{-1} after 60 cycles.

Keywords: Co_2SiO_4, cobalt orthosilicate, solid state synthesis, conversion, lithium-ion battery

***Corresponding authors**: stefano.passerini@kit.edu, dominic.bresser@kit.edu

Introduction

The steadily increasing demand for high energy storage devices for portable electronics and, recently, also for large scale applications as, for instance, electric vehicles has aroused a worldwide scientific interest in identifying and researching new active materials for lithium-ion batteries, the currently leading technology.[1–3] Regarding the anode side, these new active materials preferably offer higher specific capacities than the state-of-the-art anode material graphite, while operating at a reasonably low potential to provide increased energy densities considering their final application in lithium-ion cells. With respect to the lithium storage mechanism, the main approaches undertaken are the electrochemical (de-)alloying of lithium (basically involving elements like silicon[4–9] or tin[10–18]) and the catalytically induced, reversible conversion of transition metal oxides[19–30], nitrides,[31–34] fluorides,[35–38] or phosphides,[39–47] reported for the first time by Poizot et al. in 2000.[48] Rather recently, the combination of these two approaches has also been proposed.[49–60]

Following the conversion approach, a class of materials, which – to the best of our knowledge – has never been considered so far, are transition metal silicates, a class of materials which is of particular mineralogical and geophysical interest due to the high abundance of fayalite structured silicates in the earth's crust.[61,62] In fact, the formation of lithium silicate, starting from silicon oxide (SiO_x, $x \leq 2$) was so far commonly considered to be irreversible.[63–70]

Herein we show, however, that this initial lithium silicate formation is reversible when starting from transition metal silicates as, for instance, cobalt silicate (Co_2SiO_4), providing a reversible specific capacity of about 600 mAh g^{-1} while at the same time showing a very promising high-rate capability.

Experimental

Co_2SiO_4 synthesis

CSO was synthesized by a conventional ceramic solid state method according to Sazonov et al..[71] Stoichiometric amounts of cobalt monoxide (CoO, Alfa Aesar, 95 %) and silicon dioxide (SiO_2,

Aldrich, 99.8 %) were manually mixed within an agate mortar. The mixed powder was pressed into pellets with a pressure of 8 tons for 2 minutes and subsequently annealed in a tubular furnace (R50/250/12, Nabertherm) at 1400 K for 48 h in air (heating rate: 100 K min^{-1}). After this initial annealing step the pellets were ground again and the procedure was repeated once.

Structural and morphological characterization

The crystal structure and phase purity of CSO were determined by means of X-ray diffraction (XRD) analysis (Bruker D8 Advance equipped with a copper X-ray tube, Cu-$K_{\alpha 1}$ radiation, λ = 154.06 pm). The morphological investigation of the powder was carried out by high resolution scanning electron microscopy (HRSEM, Carl Zeiss Auriga®) equipped with a focused-ion-beam (Oxford Instruments). For this purpose, the sample was sputtered with gold for 50 s at 20 mA using a sputter coater (Quorum Technologies PQ150T ES) in order to improve its electronic conductivity.

Electrochemical characterization

Electrodes comprising the active material, conductive carbon, and binder in a weight ratio of 75:20:5 were prepared dissolving the binding agent (sodium carboxymethylcellulose, CMC, Dow Wolff Cellulosics) in ultrapure water and subsequently adding the active material (CSO) as well as the conductive agent (carbon black, Super C65®, TIMCAL). Subsequently, the solution was homogenized utilizing a planetary ball mill (Vario-Planetary Mill Pulverisette 4, Fritsch, mixing parameters: 4x 30 min at 400/-800 rpm with 10 min rest in-between). The obtained slurry was immediately cast on dendritic copper foil (Schlenk, 99.9 %) with a wet film thickness of 120 µm. The coated electrode was dried for 10 min at 80 °C and subsequently over night at room temperature. After punching disc electrodes (ø = 12 mm) the electrodes were further dried under vacuum at 120 °C for 24 h. The active material mass loading of the electrodes ranged between 1.4 and 2.2 mg cm^{-2}.

The electrochemical performance was evaluated in three-electrode Swagelok® cells using lithium foil (Rockwood Lithium, battery grade) as counter and reference electrode. Six layers of Freudenberg FS2190 served as separator while the 1M solution of $LiPF_6$ in ethylene carbonate/diethyl carbonate

(3:7 by volume, UBE) was used as electrolyte. Cell assembly was carried out in an Ar-filled glove box (MBraun UNIlab, H_2O and O_2 content < 0.1 ppm). Prior to the electrochemical characterization the cells were allowed to rest for 24 h. Cyclic voltammetry was carried out using a VMP3 potentiostat (BioLogic), setting the reversing potentials to 0.01 and 3.0 V vs. Li/Li^+ and applying a sweep rate of 50 μV s^{-1}. Galvanostatic cycling was performed utilizing a Maccor Battery Tester 4300 at a temperature of 20 ± 1 °C, setting the cut-off potentials to 0.01 and 3.0 V vs. Li/Li^+.

In situ XRD and ex situ XPS & SEM analysis

In order to gain further insight into the reaction mechanism *in situ* XRD as well as *ex situ* X-ray photoelectron spectroscopy (XPS) and SEM analysis of pristine and cycled electrodes were performed. *In situ* XRD analysis was carried out as very recently reported by Bresser et al.[30,58] The cell was discharged potentiodynamically to 0.01 V and subsequently charged to an anodic reversing potential of 3.0 V using a VSP potentiostat (BioLogic), applying a sweep rate of 0.04 mV s^{-1}. Simultaneously, XRD measurements were conducted in a 2θ range of 20° to 45° (step size: 0.0236°, scan speed 0.0393° s^{-1}, subsequent rest step: 387 s, total scan time: 30 min). *Ex situ* XPS (KRATOS Axis Ultra HAS spectroscope endowed with a monochromatic Al K_α source) analysis of a series of electrodes at different states of charge was performed at 10 mA and 12 kV. The pass energy was adjusted to 20 eV. In order to avoid charging of the samples, a charge neutralizer was utilized. For each measurement a surface area of about 300 μm x 700 μm was analyzed. All spectra were calibrated on the amorphous carbon peak in the C 1s spectrum at 285 eV. For this purpose, CSO-based electrodes were galvanostatically cycled and cycling was stopped at different potentials. The cells were then disassembled in a glove box under Ar-atmosphere and briefly rinsed with dimethyl carbonate. Subsequently, the electrodes were dried and transferred to the XPS device without contact to air and moisture. For the *ex situ* SEM analysis, the cycled electrodes were treated analogously to those used for the *ex situ* XPS analysis. The thus prepared samples were then transferred to the SEM chamber utilizing a self-designed sample holder in order to avoid any contact to air and moisture.

Results and discussion

Co_2SiO_4 synthesis: structural & morphological characterization

The XRD pattern of the synthesized CSO sample is presented in **Figure 1**. A comparison with the JCPDS reference (JCPDS card No. 01-076-1501) reveals the orthorhombic α-Co_2SiO_4 structure with the *Pbnm* space group. Since no additional reflections are observed, the material can be considered as phase pure within the XRD detection limits. In addition, SEM analysis was carried out. The SEM images (**Figure 2**) show micron-sized CSO particles with diameters ranging from 0.5 µm to 2.5 µm, i.e., a rather wide particle size distribution, which is, actually, expected for particles obtained by solid-state synthesis.

Cyclic voltammetry

In **Figure 3a** the first potentiodynamic sweep of a CSO-based electrode is presented. The initial cathodic sweep shows three reduction peaks at (**A**) 1.2 V, (**B**) 1.0 V, and (**C**) 0.86 V while the first anodic sweep exhibits two oxidation peaks at (**D**) 1.3 V (very weak and broad) and (**E**) 2.3 V. After the first cycle the specific current of peak (**A**) decreases significantly before it completely vanishes upon further cycling (**Figure 3b**). Considering the catalytic effect of transition metals on the electrochemical decomposition of common organic carbonate-based electrolytes,[72] peak (**A**) is assigned to the formation of the solid electrolyte interphase (SEI). The current peaks (**B**) and (**C**) are present only in the first cathodic sweep and are generally (at least in case of spinel-structured transition metal oxides) considered to be related to an initial lithium ion insertion into the crystalline lattice and the subsequent reduction of the comprised transition metal(s).[58,73] The different profile of the subsequent cathodic sweeps, showing a new current peak appearing at about 1.7 V (**Figure 3**, (**F**)), are characteristic for conversion-type electrochemical reactions with lithium, indicating the complete structural reorganization after the initial lithiation and a modified lithium uptake reaction mechanism.[29,30,58,60,73] Regarding the anodic sweep, the small feature at about 1.3 V (**Figure 3**, (**D**)) might be related to the partially reversible SEI formation,[74–78] as already observed by means of cyclic voltammetry for metallic tin.[18,79,80] Nevertheless, this assumption certainly deserves a more detailed

investigation in future studies. The main anodic peak (**E**) at about 2.3 V, however, is assigned to the re-oxidation of the comprised transition metal(s) – in the present case cobalt – which is in rather good agreement with previous studies on cobalt oxide.[20,30,81–83] Upon continuous potentiodynamic cycling the main cathodic (**F**) and anodic (**E**) peaks are shifted to higher potentials, while slightly decreasing in intensity, presumably related to a reduced electrode polarization caused by some kind of electrochemical grinding of the active material.[84] Nonetheless, the general profile of the cathodic and anodic sweep appears highly reversible upon subsequent cycles.

In situ XRD coupled with cyclic voltammetry

In order to better understand the reactions taking place upon the initial (de-)lithiation of CSO, *in situ* XRD analysis was performed coupled with a simultaneous potentiodynamic cathodic and anodic polarization of the electrode (**Figure 4**). The initial cathodic sweep exhibits basically two peaks at potentials of about 1.1 V (**A**) and 0.84 V (**C**), the latter showing a shoulder feature (**B**) at slightly higher potentials (about 0.9 V), which are in good agreement with the results of the cyclic voltammogram in **Figure 3a**. However, due to the higher electrode mass loading, and the resulting lithiation gradient, the profile of the potentiodynamic sweep shows broader peaks compared to the cyclic voltammogram. Hence, the distinction between the two peaks below 1 V is not that obvious. Considering the simultaneously performed XRD analysis of the electrode, it is obvious that changes of the pattern occur below 1.0 V, confirming the former assumption that the first cathodic peak at about 1.1 V is related to the SEI formation on the particles surface. Then, starting from around 0.9 V the intensity of the reflections begin to decrease and finally vanishes completely when the cell voltage reached the maximum peak current at 0.84 V, indicating the decomposition of the orthorhombic crystal structure. This observation confirms the previous evidence that at potentials lower than 1.0 V the comprised cobalt is reduced, presumably resulting in the formation of a lithium, silicon, and oxygen containing matrix – comparable to the formation of the lithium oxide matrix in the case of transition metal oxides.[48,57,58,74,76] A further characterization of the obtained composite will be given in the subsequent paragraph on the *ex situ* XPS study of a series of electrodes at different states of charge. Nonetheless, it appears noteworthy that no reflections appeared upon the subsequent

anodic sweep (result not shown here), indicating that the active material remained (quasi-)amorphous after the first lithiation, which is in good agreement with previous results for, e.g., cobalt oxide[48,73] or zinc ferrite[58].

Ex situ XPS and SEM investigation

In **Figure 5** the Co 2p and Si 2p spectra of the *ex situ* XPS analysis are presented. The pristine CSO-based electrode shows four overlapping features in the Co 2p spectrum (**Figure 5, left panel**) at binding energies of 805 eV, 799 eV, 790 eV, and 784 eV. The main peaks at 799 eV and 784 eV are assigned to Co $2p_{1/2}$ and Co $2p_{3/2}$, respectively, and the smaller peaks at 805 eV and 790 eV correspond to satellite peaks, resulting from shake excitations.[85,86] The difference in binding energy for the main and satellite peaks of about 6 eV is relatively low compared to pure CoO (9.5 eV),[85] which might be related to the different covalence of cobalt in cobalt silicate compared to cobalt monoxide. Regarding the oxidation state of cobalt, which is expected to be divalent, a distinction between Co^{2+} and Co^{3+} on the basis of XPS data is rather difficult due to the very low difference in binding energy of these two oxidation states.[86] Nonetheless, the XRD results revealing a phase-pure sample indicate that the maximum content of Co^{3+} cannot be substantially higher than 5%, which is roughly the detection limit of the XRD instrument. The Si 2p spectrum (**Figure 5, right panel**) of the pristine electrode exhibits basically only one peak at about 104 eV, which is assigned to tetravalent silicon (Si^{4+}).[87]

Upon lithiation to 0.5 V and further to 0.01 V the Co 2p peaks disappear. With respect to the limited detection depth of the X-ray beam, which is about 8 to 10 nm only, this is explained by the formation of a rather thick SEI layer on the particles surface, indicating that the formation of this layer starts at potentials higher than 0.5 V already. However, when the electrode is delithiated, the cobalt-related peaks reappear, although shifted to slightly lower binding energies. This observation suggests that the cobalt might not be fully re-oxidized again or the binding environment is simply different once the material is fully lithiated, which is, in fact, in good agreement with the results obtained by cyclic voltammetry (**Figure 3**). However, the reappearance of the peaks moreover confirms the partial reversibility, i.e., dissolution, of the SEI formation on CSO particles, which was

reported already for transition metal oxides.[55,74–76,78] These results are additionally verified by the XPS investigation of CSO-based electrodes subjected to a second cycle (discharge and charge), revealing that the lithium uptake mechanism of CSO is reversible after the initial lithiation process (see also **Figure 3b**).

The Si 2p spectra show basically the same phenomenon. The peaks disappear upon discharge and appear again upon the subsequent charge (delithiation) up to 3.0 V, confirming the previous conclusions derived from the XPS results for cobalt. The presence of a silicon peak at 0.5 V, at which the cobalt peaks had vanished already completely, might be a hint either that the thickness of the SEI layer at such potential is at the limit of the XPS detection limit or that particularly the comprised cobalt is responsible for the electrolyte decomposition. More remarkable, however, is the shift of the silicon peak towards significantly lower binding energies upon discharge, indicating a partial reduction upon discharge compared to the pristine material and presumably the formation of lithium silicate Li_4SiO_4, and elemental silicon to some very minor extent.[63,65,69] The formation of Li_4SiO_4 is only conceivable when starting from cobalt silicate and assuming the reduction of cobalt to the metallic state. The formation of elemental silicon, however, would have to be accompanied by the formation of some Li_2O. To clarifying this latter reaction in detail, nonetheless, complementary studies as, for instance, ^{29}Si NMR are required to gain further insight into the exact composition of this lithium-silicon-oxygen matrix. Upon the subsequent charge, the XPS peak shifts to higher binding energies again, indicating the partial re-oxidation of the silicon-comprising compound and/or simply a change of the binding environment, as proposed already for cobalt.

Finally, it should be noted, that the decreased intensity of all peaks observed for cobalt and silicon after the second cycle might result from the only partially reversible SEI formation.

This partially reversible formation of the SEI film is furthermore confirmed by *ex situ* SEM studies on cycled electrodes at different states of charge (**Figure 6**). Comparing the SEM images of a pristine electrode (**Figure 6a**) with discharged and charged electrodes clearly reveals the formation of a thick SEI layer on the CSO particles in the discharged state (**Figure 6b and d**, showing two electrodes discharged once and twice, respectively), which vanishes substantially upon charge (**Figure 6c and e**, showing two electrodes charged once and twice, respectively). Using the FIB, a

cross-sectional analysis of the SEI layer on a CSO particle after the first discharge was performed, showing that the thickness of this film is about 10-20 nm (**Figure 6f**).

Galvanostatic electrochemical characterization & proposal of a reaction mechanism

The reversible lithium storage capability of Co_2SiO_4 was investigated by means of galvanostatic cycling (**Figure 7**). In **Figure 7a** the potential profile of the first cycle is presented. Upon discharge two rather short plateaus at (**A**) 1.2 V and (**B**) 1.0-1.1 V and a very pronounced plateau at (**C**) 0.9-1.0 V are observed, being in good agreement with the cathodic peaks observed by performing cyclic voltammetry (**Figure 3**). Accordingly, (**A**), (**B**), and (**C**) are presumably related to the electrolyte decomposition induced by the catalytic properties of the active material, the initial lithium ion insertion into the orthorhombic host lattice, and the subsequent decomposition of the crystalline structure, respectively. Assuming the formation of Li_4SiO_4 as the main electrochemical reaction, which theoretically provides a specific capacity of 510.6 mAh g^{-1}, the result is in very good agreement with the capacity obtained for (**B**) and (**C**) only. After the third potential plateau at about 0.9-1.0 V the potential decreases steadily further, finally reaching a discharge capacity of 906.0 mAh g^{-1}. The additional capacity can be mainly assigned to an ongoing electrolyte decomposition as reported for cobalt oxide by Ponrouch et al.[78] Upon the subsequent charge, only one rather slopy plateau at about 2.2 V (**E**) is observed, being again in line with the cyclic voltammetry results (**Figure 3**).The very minor anodic peak at about 1.3 V (**D**) is presumably simply too low in intensity to be clearly observed in the potential profile of the charge step. After the first lithiation, the discharge process shows a completely changed profile with a new – although rather slopy – potential plateau at about 1.9 to 1.7 V, while the charge profile basically remains the same (**Figure 7b**; see also **Figure 3b**). However, upon continuous cycling the two potential plateaus upon discharge and charge are getting less and less distinct (as indicated by the left arrow in **Figure 7b**) and the charge and discharge potential profiles become more and more slopy, which is also in good agreement with the decreasing current intensity observed by the continuous potentiodynamic cycling (**Figure 3 b**). Besides, the reversible specific capacity of initially 592 mAh g^{-1} is increasing with an increasing cycle number, finally reaching 652 mAh g^{-1} after 60 cycles (indicated by the upper right

arrow in **Figure 7b**). This additional capacity is mainly obtained in the potential region below 0.7 V, confirming the assumption of the reversible formation of a polymeric layer on the CSO particles already evidenced by *ex situ* XPS and SEM (**Figure 5 and 6**, respectively). A similar phenomenon was, indeed, already reported in literature for transition metal oxides[74,78,88] as well as combined conversion/alloying materials[56,58]. In **Figure 7c** the specific capacity is plotted vs. the cycle number, once again showing the highly reversible cycling behavior, a high coulombic efficiency of about 99 %, and the increasing specific capacity upon continuous (dis-)charge of the electrode.

Considering now, all the herein described results, the following reaction mechanism for the reversible lithium storage of cobalt orthosilicate (Co_2SiO_4) is proposed:

(1) First discharge: $Co_2SiO_4 + 4\ Li^+ + 4\ e^- \rightarrow 2\ Co^0 + Li_4SiO_4$

(2) Subsequent charge/discharge: $x\ Co^0 + Li_4SiO_4 \leftrightarrow 4\ Li^+ + 4\ e^- + Co_xSiO_y$

As mentioned in the introduction, the formation of lithium silicate (Li_4SiO_4), starting from SiO_x ($X \leq 2$) was so far considered to be irreversible.[63–70] However, by starting from a transition metal silicate, as for instance, cobalt silicate, as presented herein, the formation of Li_4SiO_4 appears to be reversible, supposably enabled by the initial formation of metallic cobalt nanograins as reported first for transition metal oxides by Poizot et al.[48] in 2000. Additional electrochemical reactions as, for instance, the partial reduction to elemental silicon and its alloying with lithium are certainly also possible. However, from the herein presented results there is no hint on such reactions and/or the formation of elemental silicon or its lithium alloy. Thus, at least the complete reduction of CSO to metallic cobalt and elemental silicon can be discarded.

As a last step, the rate performance of CSO-based electrodes was studied by applying elevated specific currents, i.e., 0.08 A g^{-1}, 0.16 A g^{-1}, 0.32 A g^{-1}, 0.79 A g^{-1}, 1.58 A g^{-1}, 3.17 A g^{-1}, and 7.19 A g^{-1}. **Figure 8a** shows the results of this multi-rate test and **Figure 8b** the corresponding potential profiles. The reversible specific capacities delivered at the fifth cycle for each rate were 575 mAh g^{-1} (0.08 A g^{-1}), 576 mAh g^{-1} (0.16 A g^{-1}), 548 mAh g^{-1} (0.32 A g^{-1}), 477 mAh g^{-1}

(0.79 A g^{-1}), 370 mAh g^{-1} (1.58 A g^{-1}), 238 mAh g^{-1} (3.17 A g^{-1}), and 83 mAh g^{-1} (7.91 A g^{-1}). It is quite remarkable that the specific capacity at a rather high specific current of 1.58 A g^{-1} (370 mAh g^{-1}, i.e., 64.3% of the initial reversible capacity) is still as high as the theoretical capacity of graphite, while the applied current would correspond to a C rate of more than 4C for this state-of-the-art anode material. In regard to the proposed reaction mechanism, this very interesting high rate capability of CSO – particularly considering the relatively large particle size – might be related to the good lithium ion conductivity of the formed lithium silicate phase Li_4SiO_4.[89] Nevertheless, the basic reason for the capacity decrease at elevated C rates is obviously an increasing polarization (**Figure 8b**). However, this might be addressed in future by the utilization of nanosized particles, increasing the electrode/electrolyte contact area and, hence, reducing the applied current density per unit surface area, and/or by embedding such particles in electronically conductive matrices. Finally, the very good capacity retention of 579 mAh g^{-1} at 0.16 A g^{-1} after applying such high currents appears noteworthy.

Conclusions

Co_2SiO_4 was synthesized by a common solid-state method and characterized morphologically, structurally, and electrochemically with respect to its application as lithium-ion active material. Cyclic voltammetry experiments indicated a conversion-type electrochemical reaction with lithium, based on the reversible formation of lithium silicate (Li_4SiO_4), which was confirmed by *in situ* XRD, *ex situ* XPS and SEM, as well as galvanostatic electrochemical analysis of electrodes comprising cobalt silicate as active material. In addition, the partially reversible formation of the continuously formed SEI layer on the CSO particles, having a thickness of about 10 to 20 nm was confirmed, being the reason for a slight increase of the specific capacity upon cycling. Indeed, micron-sized CSO particles show a highly stable lithium storage capability and, in addition, a very interesting high rate capability, particularly considering the rather large particle size.

These results might trigger further studies on other transition metal silicates, having an optimized particle morphology and size, as well as composites containing a conductive matrix for such silicates in order to further improve their electrochemical performance and, in particular, their high rate capability. Moreover, considering previous studies on conversion-type materials, a similar reaction

mechanism is expected to occur for iron and manganese silicate with lithium at low potentials. These silicates are of particular interest since the analogous lithium transition metal silicates are currently investigated as potential candidates for lithium-ion cathodes.

Acknowledgments

Financial support from the European Commission within the ORION (229036) and the AMELIE (265910) project under the Seventh Framework Program (7^{th} FWP) is gratefully acknowledged. TIMCAL, Rockwood Lithium, Freudenberg, and DOW Wolff Cellulosic are kindly acknowledged for providing CMC, lithium metal, polypropylene separator, and Super C65, respectively.

References

1. M. Armand and J.-M. Tarascon, *Nature*, 2008, **451**, 652–657.
2. B. Scrosati and J. Garche, *J. Power Sources*, 2010, **195**, 2419–2430.
3. B. Scrosati, J. Hassoun, and Y.-K. Sun, *Energy Environ. Sci.*, 2011, **4**, 3287–3295.
4. C. K. Chan, H. Peng, G. Liu, K. McIlwrath, X. F. Zhang, R. A. Huggins, and Y. Cui, *Nat Nano*, 2008, **3**, 31–35.
5. J. Graetz, C. C. Ahn, R. Yazami, and B. Fultz, *Electrochem. Solid-State Lett.*, 2003, **6**, A194–A197.
6. M. Gu, Y. Li, X. Li, S. Hu, X. Zhang, W. Xu, S. Thevuthasan, D. R. Baer, J.-G. Zhang, J. Liu, and C. Wang, *ACS Nano*, 2012, **6**, 8439–8447.
7. B. Gao, S. Sinha, L. Fleming, and O. Zhou, *Adv. Mater.*, 2001, **13**, 816–819.
8. M. Holzapfel, H. Buqa, L. J. Hardwick, M. Hahn, A. Würsig, W. Scheifele, P. Novák, R. Kötz, C. Veit, and F.-M. Petrat, *Electrochimica Acta*, 2006, **52**, 973–978.
9. S. D. Beattie, D. Larcher, M. Morcrette, B. Simon, and J.-M. Tarascon, *J. Electrochem. Soc.*, 2008, **155**, A158–A163.
10. A. N. Dey, *J. Electrochem. Soc.*, 1971, **118**, 1547–1549.
11. J. Wang, P. King, and R. A. Huggins, *Solid State Ion.*, 1986, **20**, 185–189.
12. J. O. Besenhard, M. Hess, and P. Komenda, *Solid State Ion.*, 1990, **40–41, Part 2**, 525–529.
13. M. Winter and J. O. Besenhard, *Electrochimica Acta*, 1999, **45**, 31–50.
14. M. Wachtler, J. O. Besenhard, and M. Winter, *Spec. Issue Interfacial Phenom. Batter.*, 2001, **94**, 189–193.
15. D. Larcher, S. Beattie, M. Morcrette, K. Edstrom, J.-C. Jumas, and J.-M. Tarascon, *J Mater Chem*, 2007, **17**, 3759–3772.
16. G. Derrien, J. Hassoun, S. Panero, and B. Scrosati, *Adv. Mater.*, 2007, **19**, 2336–2340.
17. J. Hassoun, G. Derrien, S. Panero, and B. Scrosati, *Adv. Mater.*, 2008, **20**, 3169–3175.
18. D. Bresser, F. Mueller, D. Buchholz, E. Paillard, and S. Passerini, *Electrochimica Acta*, 2014, **128**, 163–171.
19. J.-M. Tarascon, S. Grugeon, M. Morcrette, S. Laruelle, P. Rozier, and P. Poizot, *Comptes Rendus Chim.*, 2005, **8**, 9–15.
20. G. X. Wang, Y. Chen, K. Konstantinov, M. Lindsay, H. K. Liu, and S. X. Dou, *J. Power Sources*, 2002, **109**, 142–147.
21. P. L. Taberna, S. Mitra, P. Poizot, P. Simon, and J.-M. Tarascon, *Nat. Mater.*, 2006, **5**, 567–573.
22. S. Mitra, P. Poizot, A. Finke, and J.-M. Tarascon, *Adv. Funct. Mater.*, 2006, **16**, 2281–2287.
23. C. Vidal-Abarca, P. Lavela, and J. L. Tirado, *Electrochem. Solid-State Lett.*, 2008, **11**, A198–A201.
24. J. Li, H. M. Dahn, L. J. Krause, D.-B. Le, and J. R. Dahn, *J. Electrochem. Soc.*, 2008, **155**, A812–A816.
25. M. R. Palacin, *Chem. Soc. Rev.*, 2009, **38**, 2565–2575.
26. J. Cabana, L. Monconduit, D. Larcher, and M. R. Palacín, *Adv. Mater.*, 2010, **22**, E170–E192.
27. X. Wang, Z. Yang, X. Sun, X. Li, D. Wang, P. Wang, and D. He, *J. Mater. Chem.*, 2011, **21**, 9988–9990.
28. M. V. Reddy, G. V. Subba Rao, and B. V. R. Chowdari, *Chem. Rev.*, 2013, **113**, 5364–5457.
29. A. Brandt and A. Balducci, *J. Power Sources*, 2013, **230**, 44–49.
30. D. Bresser, E. Paillard, P. Niehoff, S. Krueger, F. Mueller, M. Winter, and S. Passerini, *ChemPhysChem*, 2014, DOI: 10.1002/cphc.201400092.
31. Y. Wang, Z.-W. Fu, X.-L. Yue, and Q.-Z. Qin, *J. Electrochem. Soc.*, 2004, **151**, E162–E167.
32. Z.-W. Fu, Y. Wang, X.-L. Yue, S.-L. Zhao, and Q.-Z. Qin, *J. Phys. Chem. B*, 2004, **108**, 2236–2244.
33. F. Gillot, J. Oro-Sole, and M. R. Palacin, *J. Mater. Chem.*, 2011, **21**, 9997–10002.
34. B. Das, M. V. Reddy, G. V. S. Rao, and B. V. R. Chowdari, *J. Mater. Chem.*, 2012, **22**, 17505–17510.
35. F. Badway, N. Pereira, F. Cosandey, and G. G. Amatucci, *J. Electrochem. Soc.*, 2003, **150**, A1209–A1218.
36. F. Badway, F. Cosandey, N. Pereira, and G. G. Amatucci, *J. Electrochem. Soc.*, 2003, **150**, A1318–A1327.
37. Z.-W. Fu, C.-L. Li, W.-Y. Liu, J. Ma, Y. Wang, and Q.-Z. Qin, *J. Electrochem. Soc.*, 2005, **152**, E50–E55.
38. S.-W. Kim, D.-H. Seo, H. Gwon, J. Kim, and K. Kang, *Adv. Mater.*, 2010, **22**, 5260–5264.

39. R. Alcántara, J. . Tirado, J. . Jumas, L. Monconduit, and J. Olivier-Fourcade, *J. Power Sources*, 2002, **109**, 308–312.
40. D. C. C. Silva, O. Crosnier, G. Ouvrard, J. Greedan, A. Safa-Sefat, and L. F. Nazar, *Electrochem. Solid-State Lett.*, 2003, **6**, A162–A165.
41. M. P. Bichat, T. Politova, J. L. Pascal, F. Favier, and L. Monconduit, *J. Electrochem. Soc.*, 2004, **151**, A2074–A2081.
42. H. Pfeiffer, F. Tancret, M.-P. Bichat, L. Monconduit, F. Favier, and T. Brousse, *Electrochem. Commun.*, 2004, **6**, 263–267.
43. B. Mauvernay, M.-P. Bichat, F. Favier, L. Monconduit, M. Morcrette, and M.-L. Doublet, *Ionics*, 2005, **11**, 36–45.
44. O. Crosnier and L. F. Nazar, *Electrochem. Solid-State Lett.*, 2004, **7**, A187–A189.
45. V. Pralong, D. C. S. Souza, K. T. Leung, and L. F. Nazar, *Electrochem. Commun.*, 2002, **4**, 516–520.
46. J. Y. Xiang, X. L. Wang, J. Zhong, D. Zhang, and J. P. Tu, *J. Power Sources*, 2011, **196**, 379–385.
47. M. C. Stan, R. Klöpsch, A. Bhaskar, J. Li, S. Passerini, and M. Winter, *Adv. Energy Mater.*, 2013, **3**, 231–238.
48. P. Poizot, S. Laruelle, S. Grugeon, L. Dupont, and J.-M. Tarascon, *Nature*, 2000, **407**, 496–499.
49. Y.-N. NuLi, Y.-Q. Chu, and Q.-Z. Qin, *J. Electrochem. Soc.*, 2004, **151**, A1077–A1083.
50. Y. Sharma, N. Sharma, G. V. Subba Rao, and B. V. R. Chowdari, *Adv. Funct. Mater.*, 2007, **17**, 2855–2861.
51. Y. Sharma, N. Sharma, G. V. S. Rao, and B. V. R. Chowdari, *Electrochimica Acta*, 2008, **53**, 2380–2385.
52. X. Guo, X. Lu, X. Fang, Y. Mao, Z. Wang, L. Chen, X. Xu, H. Yang, and Y. Liu, *Electrochem. Commun.*, 2010, **12**, 847–850.
53. Y. Deng, Q. Zhang, S. Tang, L. Zhang, S. Deng, Z. Shi, and G. Chen, *Chem Commun*, 2011, **47**, 6828–6830.
54. Y. Ding, Y. Yang, and H. Shao, *Electrochimica Acta*, 2011, **56**, 9433–9438.
55. B. Liu, J. Zhang, X. Wang, G. Chen, D. Chen, C. Zhou, and G. Shen, *Nano Lett.*, 2012, **12**, 3005–3011.
56. F. Mueller, D. Bresser, E. Paillard, M. Winter, and S. Passerini, *J. Power Sources*, 2013, **236**, 87–94.
57. D. Bresser, F. Mueller, M. Fiedler, S. Krueger, R. Kloepsch, D. Baither, M. Winter, E. Paillard, and S. Passerini, *Chem. Mater.*, 2013, **25**, 4977–4985.
58. D. Bresser, E. Paillard, R. Kloepsch, S. Krueger, M. Fiedler, R. Schmitz, D. Baither, M. Winter, and S. Passerini, *Adv. Energy Mater.*, 2013, **3**, 513–523.
59. A. Varzi, D. Bresser, J. von Zamory, F. Mueller, and S. Passerini, *Adv. Energy Mater.*, 2014, DOI: 10.1002/aenm.201400054.
60. F. Martinez-Julian, A. Guerrero, M. Haro, J. Bisquert, D. Bresser, E. Paillard, S. Passerini, and G. Garcia-Belmonte, *J. Phys. Chem. C*, 2014, **118**, 6069–6076.
61. X. Jiang and G. Y. Guo, *Int. Symp. Adv. Magn. Technol.*, 2004, **282**, 287–290.
62. A. Sazonov, M. Meven, V. Hutanu, G. Heger, T. Hansen, and A. Gukasov, *Acta Crystallogr. Sect. B*, 2009, **65**, 664–675.
63. M. Miyachi, H. Yamamoto, H. Kawai, T. Ohta, and M. Shirakata, *J. Electrochem. Soc.*, 2005, **152**, A2089–A2091.
64. X. Yang, Z. Wen, X. Xu, B. Lin, and S. Huang, *J. Power Sources*, 2007, **164**, 880–884.
65. B. Guo, J. Shu, Z. Wang, H. Yang, L. Shi, Y. Liu, and L. Chen, *Electrochem. Commun.*, 2008, **10**, 1876–1878.
66. A. Veluchamy, C.-H. Doh, D.-H. Kim, J.-H. Lee, D.-J. Lee, K.-H. Ha, H.-M. Shin, B.-S. Jin, H.-S. Kim, S.-I. Moon, and C.-W. Park, *J. Power Sources*, 2009, **188**, 574–577.
67. J. Wang, H. Zhao, J. He, C. Wang, and J. Wang, *J. Power Sources*, 2011, **196**, 4811–4815.
68. W.-S. Chang, C.-M. Park, J.-H. Kim, Y.-U. Kim, G. Jeong, and H.-J. Sohn, *Energy Environ. Sci.*, 2012, **5**, 6895–6899.
69. N. Yan, F. Wang, H. Zhong, Y. Li, Y. Wang, L. Hu, and Q. Chen, *Sci Rep*, 2013, **3**.
70. Y. Hwa, C.-M. Park, and H.-J. Sohn, *J. Power Sources*, 2013, **222**, 129–134.
71. A. P. Sazonov, PhD Thesis, RWTH Aachen, 2009.
72. J.-S. Bridel, S. Grugeon, S. Laruelle, J. Hassoun, P. Reale, B. Scrosati, and J.-M. Tarascon, *J. Power Sources*, 2010, **195**, 2036–2043.

73. D. Larcher, G. Sudant, J.-B. Leriche, Y. Chabre, and J.-M. Tarascon, *J. Electrochem. Soc.*, 2002, **149**, A234–A241.
74. P. Poizot, S. Laruelle, S. Grugeon, L. Dupont, and J.-M. Tarascon, *Ionics*, 2000, **6**, 321–330.
75. S. Laruelle, S. Grugeon, P. Poizot, M. Dollé, L. Dupont, and J.-M. Tarascon, *J. Electrochem. Soc.*, 2002, **149**, A627–A634.
76. S. Grugeon, S. Laruelle, L. Dupont, and J.-M. Tarascon, *Solid State Sci.*, 2003, **5**, 895–904.
77. R. Dedryvère, S. Laruelle, S. Grugeon, P. Poizot, D. Gonbeau, and J.-M. Tarascon, *Chem Mater*, 2004, **16**, 1056–1061.
78. A. Ponrouch, P.-L. Taberna, P. Simon, and M. R. Palacín, *Electrochimica Acta*, 2012, **61**, 13–18.
79. B. Guo, J. Shu, K. Tang, Y. Bai, Z. Wang, and L. Chen, *J. Power Sources*, 2008, **177**, 205–210.
80. X. W. Guo, X. P. Fang, Y. Sun, L. Y. Shen, Z. X. Wang, and L. Q. Chen, *J. Power Sources*, 2013, **226**, 75–81.
81. W. Y. Li, L. N. Xu, and J. Chen, *Adv. Funct. Mater.*, 2005, **15**, 851–857.
82. N. Jayaprakash, W. D. Jones, S. S. Moganty, and L. A. Archer, *J. Power Sources*, 2012, **200**, 53–58.
83. F. Wang, C. Lu, Y. Qin, C. Liang, M. Zhao, S. Yang, Z. Sun, and X. Song, *J. Power Sources*, 2013, **235**, 67–73.
84. G. Binotto, D. Larcher, A. S. Prakash, R. Herrera Urbina, M. S. Hegde, and J.-M. Tarascon, *Chem. Mater.*, 2007, **19**, 3032–3040.
85. B. Mayer, S. Uhlenbrock, and M. Neumann, *J. Electron Spectrosc. Relat. Phenom.*, 1996, **81**, 63–67.
86. W. Wang and G. Zhang, *J. Cryst. Growth*, 2009, **311**, 4275–4280.
87. K. Joong Kim, K. T. Park, and J. W. Lee, *Thin Solid Films*, 2006, **500**, 356–359.
88. F. Badway, I. Plitz, S. Grugeon, S. Laruelle, M. Dollé, A. S. Gozdz, and J.-M. Tarascon, *Electrochem. Solid-State Lett.*, 2002, **5**, A115–A118.
89. S. Xun, X. Song, L. Wang, M. E. Grass, Z. Liu, V. S. Battaglia, and G. Liu, *J. Electrochem. Soc.*, 2011, **158**, A1260–A1266.

Co_2SiO_4 is investigated for the first time as lithium-ion active material and a lithium storage mechanism is proposed including the reversible formation of Li_4SiO_4.

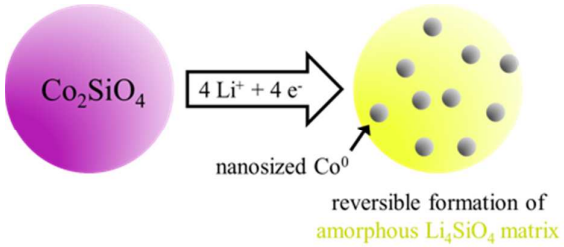

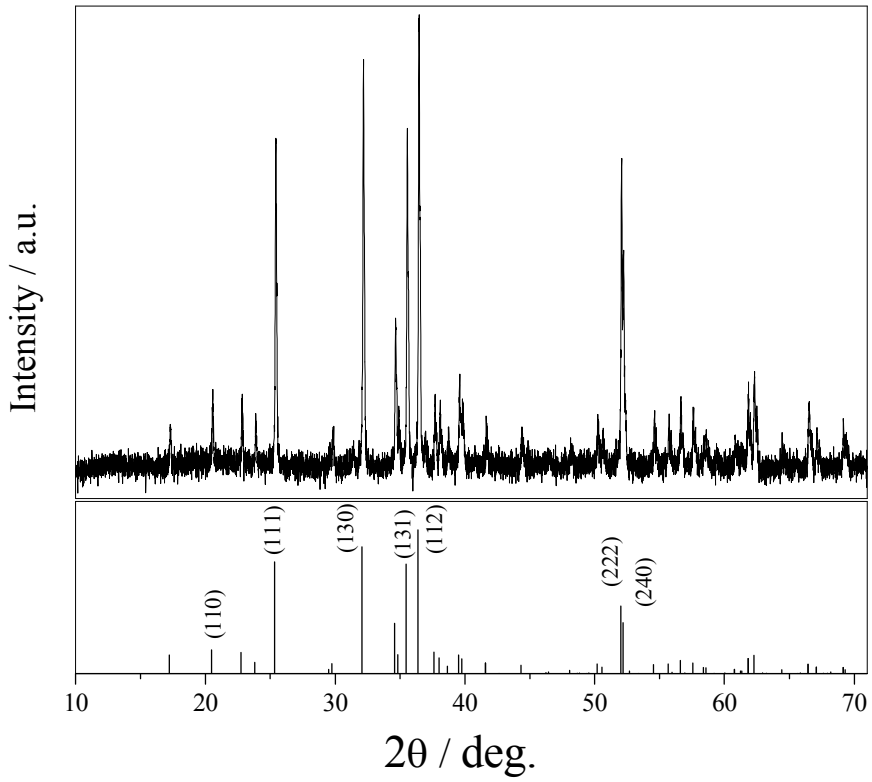

Figure 1. XRD pattern of as-synthesized CSO; as reference given in the bottom: JCPDS card No. 01-076-1501.

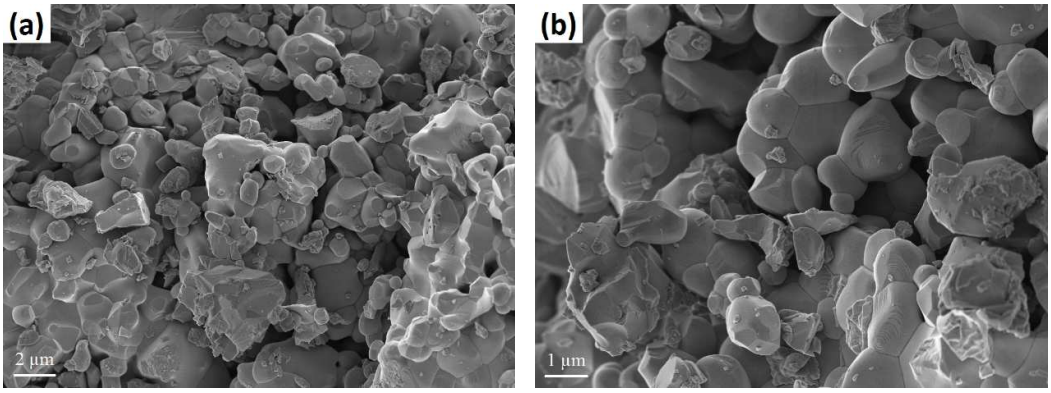

Figure 2. SEM images of as-synthesized CSO at a magnification of (a) 5kx and (b) 10kx.

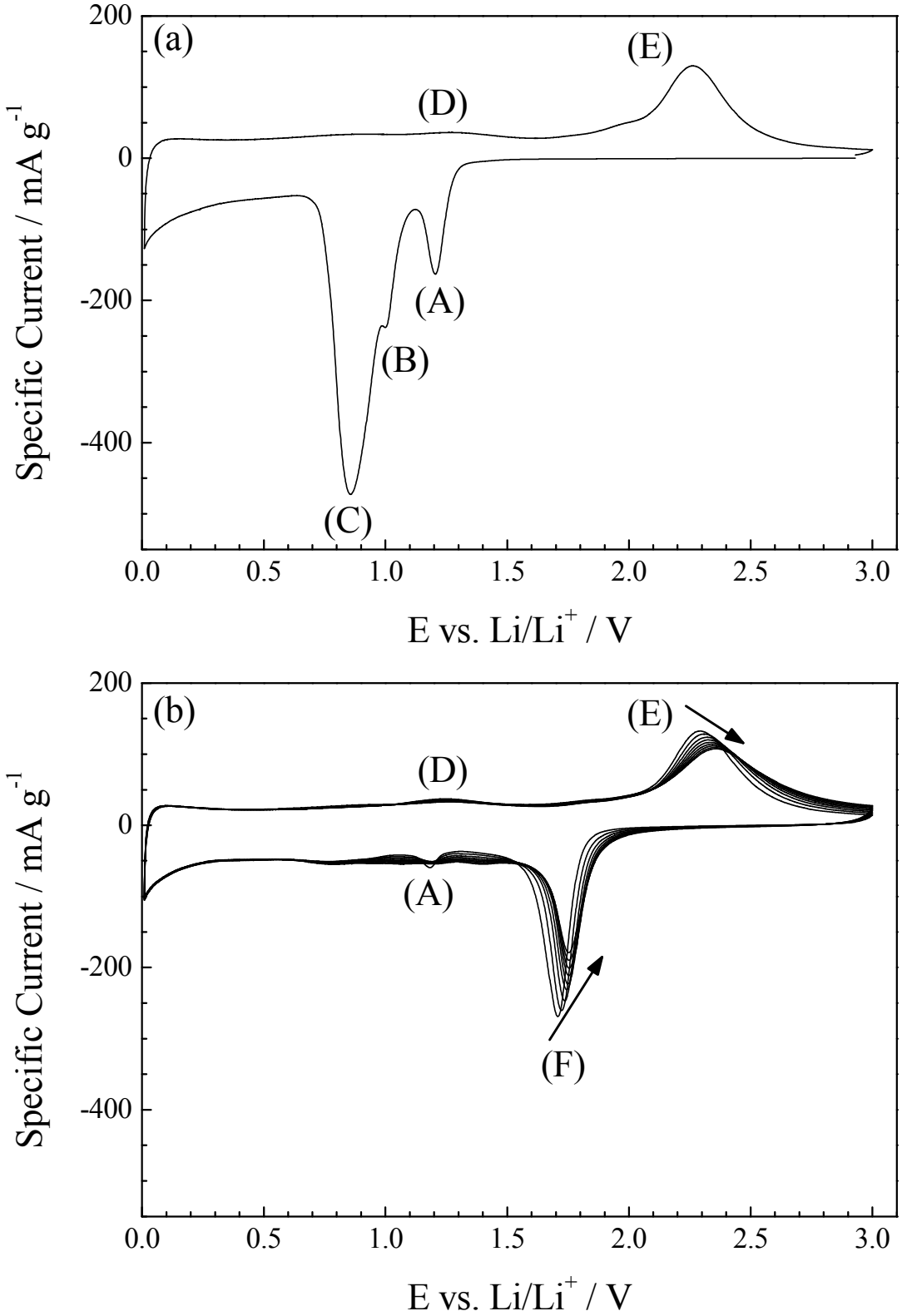

Figure 3. Cyclic voltammograms of CSO-based electrodes: (a) 1st sweep. (b) 2nd to 10th sweep. Sweep rate: 50 μV s^{-1}, reversing potentials: 0.01 V and 3.0 V vs. Li/Li^+.

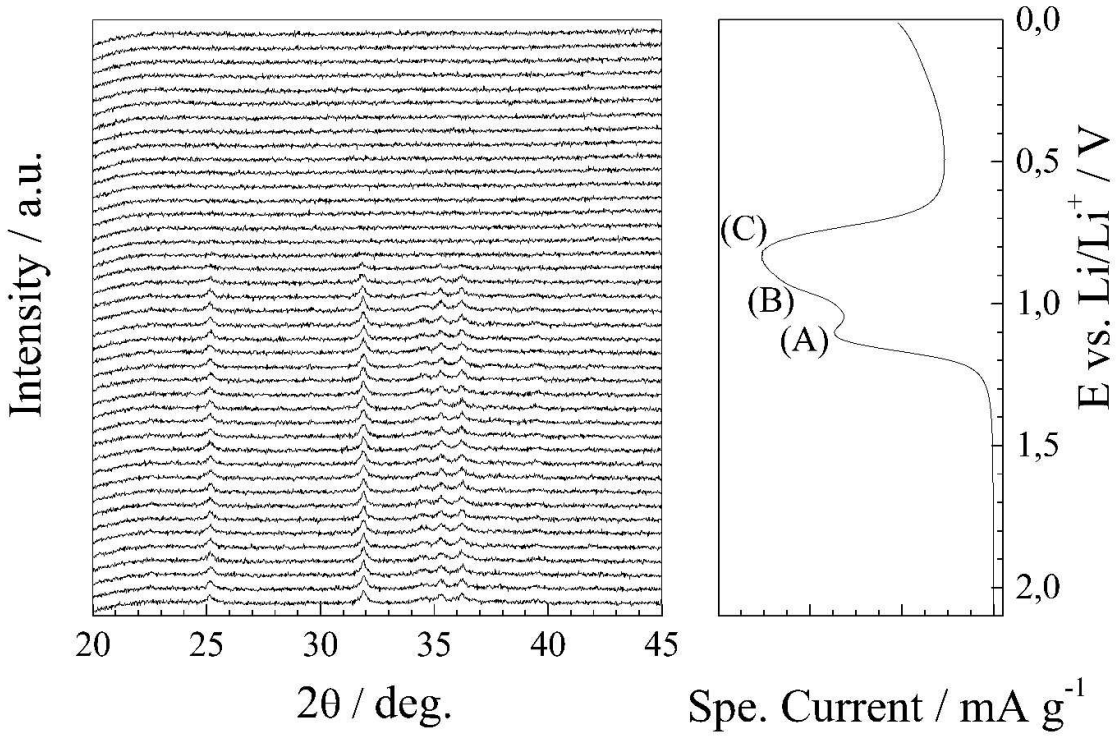

Figure 4. *In situ* XRD analysis of a CSO-based electrode: left panel: waterfall diagram of consecutively recorded XRD patterns in a 2θ range of 20° to 45°; right panel: the corresponding plot of the specific current vs. potential for the 1st lithiation.

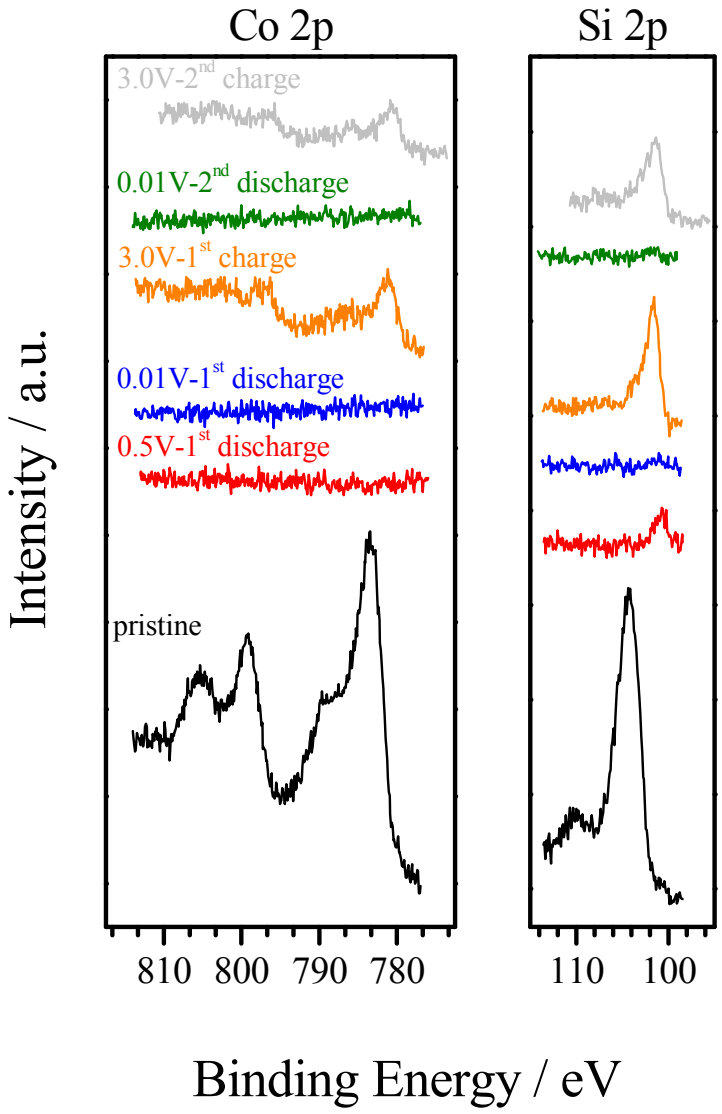

Figure 5. Co 2p and Si 2p XPS spectra of CSO-based electrodes at different states of charge.

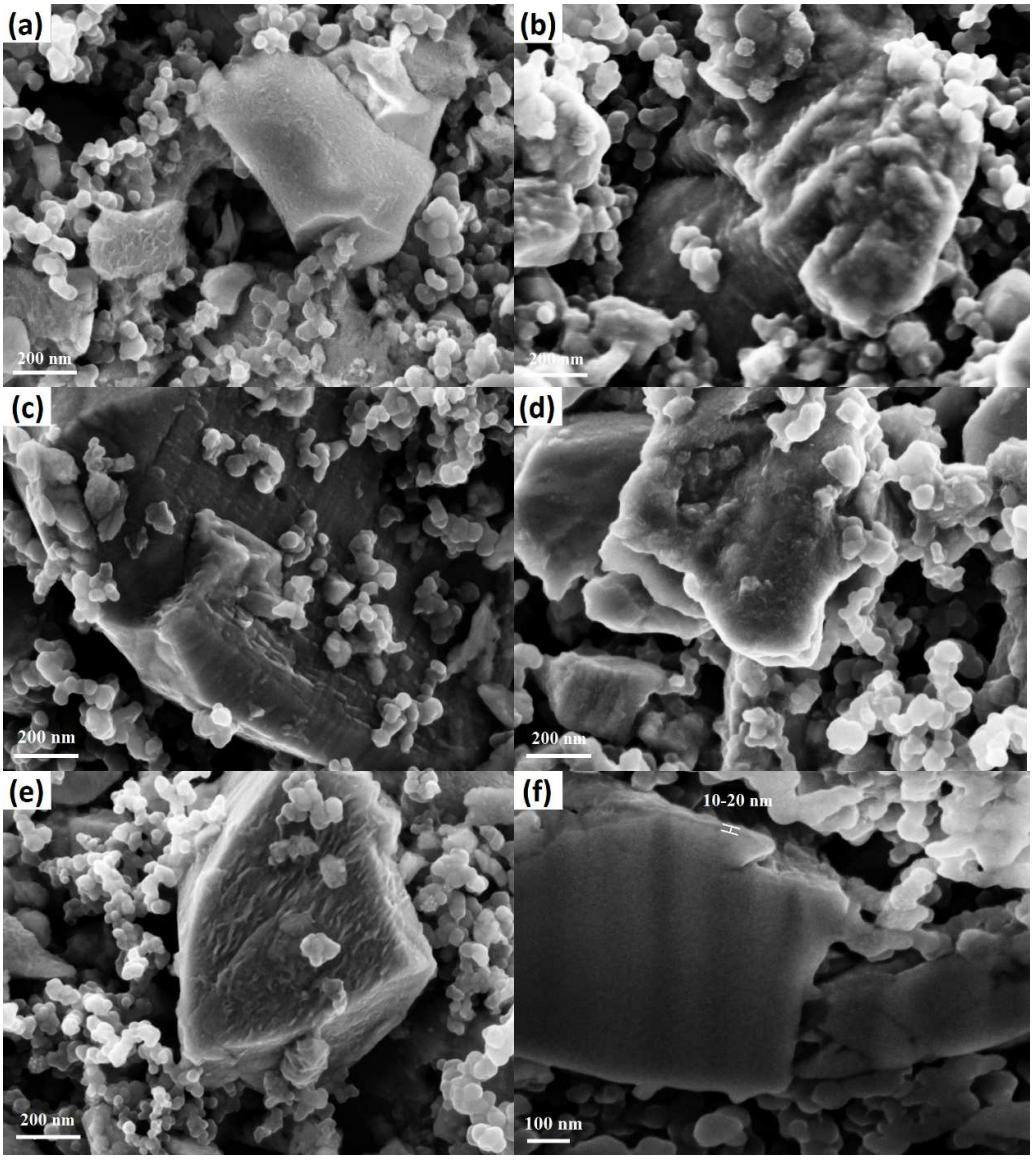

Figure 6. SEM images of CSO-based electrodes: (a) pristine electrode (magnification 75kx); (b) after the 1st discharge (magnification 75kx); (c) after the 1st charge (magnification 75kx); (d) after the 2nd discharge (magnification 75kx); (e) after the 2nd charge (magnification 75kx); (f) cross section after the 1st discharge (magnification 100kx).

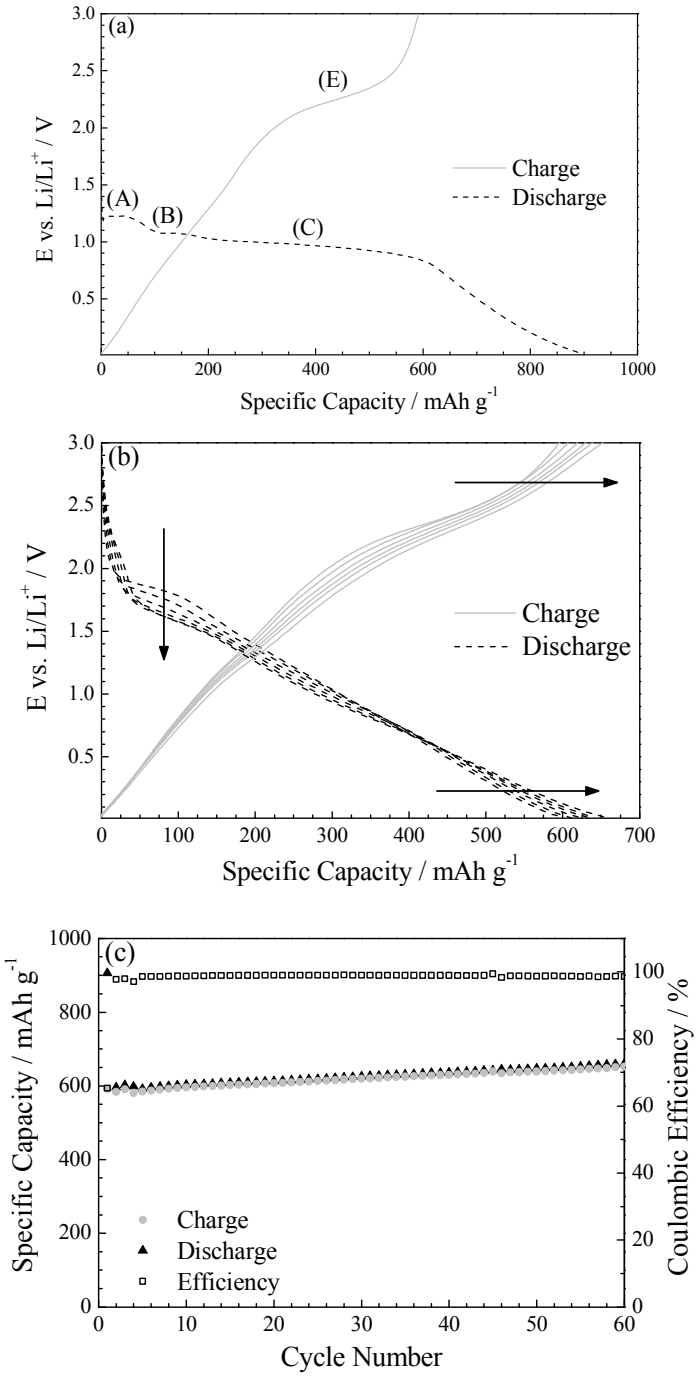

Figure 7. Electrochemical galvanostatic investigation of CSO-based electrodes: (a) potential profile of the 1st cycle (specific current: 80 mA g^{-1}); (b) potential profiles of each 10th cycle (specific current: 160 mA g^{-1}); (c) specific capacity vs. cycle number, including three formation cycles at 80 mA g^{-1}, followed by constant current cycling at 160 mA g^{-1}; cut-off potentials: 0.01 V and 3.0 V vs. Li/Li^+.

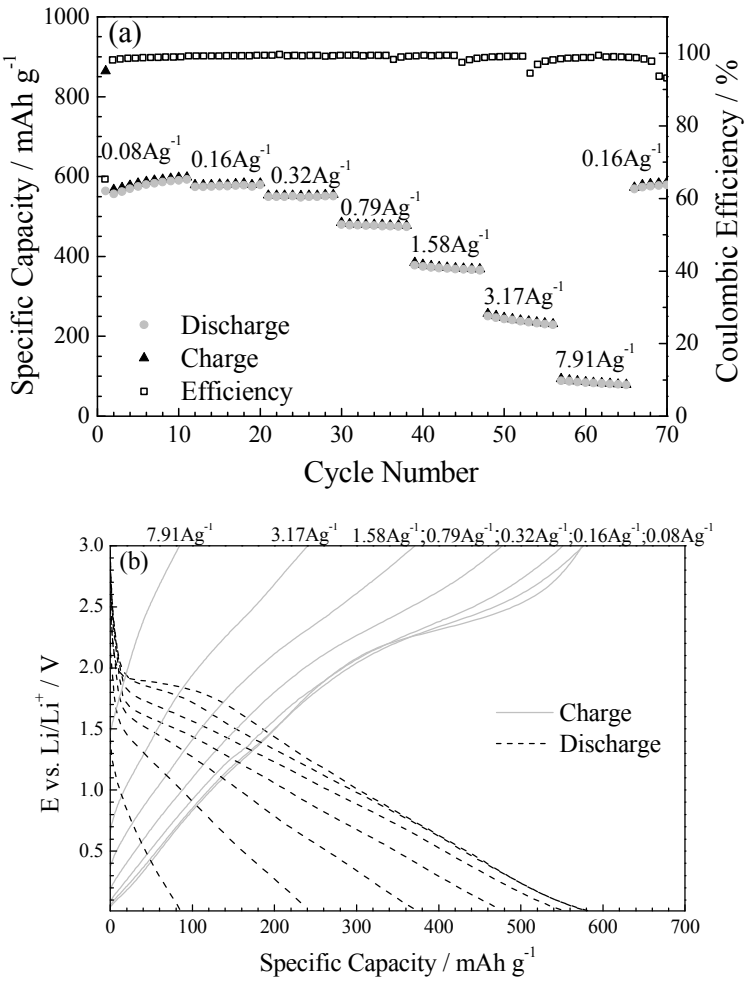

Figure 8. Multi-rate galvanostatic cycling of CSO-based electrodes: (a) specific capacity vs. cycle number, including two formation cycles at 0.08 A g^{-1} (i.e., 80 mA g^{-1}), followed by each 10 cycles at 0.08 A g^{-1}, 0.16 A g^{-1}, 0.32 A g^{-1}, 0.79 A g^{-1}, 1.58 A g^{-1}, 3.17 A g^{-1}, and 7.91 A g^{-1}; subsequently, the applied specific current was decreased back to 0.16 A g^{-1}; (b) corresponding potential profiles at different specific currents (0.08 A g^{-1}, 0.16 A g^{-1}, 0.32 A g^{-1}, 0.79 A g^{-1}, 1.58 A g^{-1}, 3.17 A g^{-1}, and 7.91 A g^{-1}); cut-off potentials: 0.01 V and 3.0 V vs. Li/Li^+.